

Boundary layer state detection using piezoelectric sensors

Stuber, Vincent L.; Kotsonis, Marios; Van Der Zwaag, Sybrand

DOI

[10.1088/1361-665X/ac3900](https://doi.org/10.1088/1361-665X/ac3900)

Publication date

2022

Document Version

Final published version

Published in

Smart Materials and Structures

Citation (APA)

Stuber, V. L., Kotsonis, M., & Van Der Zwaag, S. (2022). Boundary layer state detection using piezoelectric sensors. *Smart Materials and Structures*, 31(1), Article 015014. <https://doi.org/10.1088/1361-665X/ac3900>

Important note

To cite this publication, please use the final published version (if applicable).
Please check the document version above.

Copyright

Other than for strictly personal use, it is not permitted to download, forward or distribute the text or part of it, without the consent of the author(s) and/or copyright holder(s), unless the work is under an open content license such as Creative Commons.

Takedown policy

Please contact us and provide details if you believe this document breaches copyrights.
We will remove access to the work immediately and investigate your claim.

PAPER • OPEN ACCESS

Boundary layer state detection using piezoelectric sensors

To cite this article: Vincent L Stuber *et al* 2022 *Smart Mater. Struct.* **31** 015014

View the [article online](#) for updates and enhancements.

You may also like

- [Effect of grain boundary on martensite transformation behaviour in Fe-32 at.%Ni bicrystals](#)
Masato Ueda, Hiroyuki Yasuda and Yukichi Umakoshi
- [Grain boundary migration in Fe-3mass%Si alloy bicrystals with twist boundary](#)
T Shibayanagi, K Ichimiya and Y Umakoshi
- [On the Utility of Constant Phase Elements to Characterize Heterogeneous Ceramic Grain Boundaries](#)
Benjamin E. McNealy and Joshua L. Hertz



The Electrochemical Society
Advancing solid state & electrochemical science & technology

242nd ECS Meeting

Oct 9 – 13, 2022 • Atlanta, GA, US

Abstract submission deadline: **April 8, 2022**

Connect. Engage. Champion. Empower. Accelerate.

MOVE SCIENCE FORWARD



Submit your abstract



Boundary layer state detection using piezoelectric sensors

Vincent L Stuber^{*} , Marios Kotsonis  and Sybrand van der Zwaag

Delft University of Technology, Kluyverweg 1, 2629 HS Delft, The Netherlands

E-mail: V.L.Stuber@tudelft.nl

Received 26 March 2021, revised 30 September 2021

Accepted for publication 11 November 2021

Published 23 November 2021



CrossMark

Abstract

Two piezoelectric series bimorph sensors were embedded below the skin of a NACA 0012 symmetrical airfoil to detect the local state of the boundary layer during wind tunnel testing. Small vanes piercing the airfoil skin were glued onto the bimorphs providing a mechanical coupling to the local mechanical force fluctuations imparted by the local unsteady boundary layer flow. The state of the boundary layer at the sensor sites was varied by changing the angle of attack. The objective of this work was to establish the ability of this sensor concept to accurately distinguish among typical boundary layer states such as attached laminar flow, turbulent flow and separated flow. The output of the sensor was compared to concurrent time-resolved particle image velocimetry measurements, which served as a validation technique. Using the developed sensor response envelope, a single data point time series of the piezo electrical signal was proven to be sufficient to accurately detect the boundary layer state on classical airfoils in the low Reynolds number regime. In projected future applications, single or arrays of bimorph sensors can be used to map the boundary layer of more complex or morphing shape airfoils. The fast response of the sensor can in principle be utilised in closed-loop flow control systems, aimed at drag reduction or lift enhancement.

Keywords: piezoelectricity, laminar-to-turbulent transition, separation, wind tunnel experiments, particle image velocimetry

(Some figures may appear in colour only in the online journal)

1. Introduction

The boundary layer plays an important role in the lift-to-drag ratio of airfoils, through the coupling of viscous and inviscid mechanisms. Typically, boundary layers can be classified as either laminar, which can be described as organised flow containing non-intersecting smoothly developing and predictable paths, or turbulent, which can be described as an almost random chaotic flow. The region in between the two states, where laminar flow changes into turbulent flow, is governed by

the so-called laminar-to-turbulent transition process, typically (but not exclusively) governed by the emergence and growth of shear layer instabilities. Laminar or turbulent, boundary layers can experience so-called detachment or separation. Then they are unable to follow the shape of the aerodynamic surface, creating large recirculating areas.

A major difference between laminar, turbulent and separated flow is the drag generated which increases continuously when going from laminar to turbulent to fully separated [1–3]. Here, turbulent flow increases skin friction drag compared to laminar flow, while separated flow increases the total pressure drag acting on the airfoil. In most aerodynamic applications, a high lift-to-drag ratio is desirable, as it leads to a higher aerodynamic efficiency. One way of increasing the lift-to-drag ratio of airfoils is to postpone transition and separation and to bring their locations as far downstream on the wing as possible. This can be achieved by passive means such as airfoil

* Author to whom any correspondence should be addressed.



Original content from this work may be used under the terms of the [Creative Commons Attribution 4.0 licence](https://creativecommons.org/licenses/by/4.0/). Any further distribution of this work must maintain attribution to the author(s) and the title of the work, journal citation and DOI.

shape optimization [4] or by active means such as applying a feedback loop to an overactuated morphing aircraft wing, or by operating micro-actuator devices such as jet or plasma actuators [5–8].

In case of active flow control techniques, proper performance of such a feedback loop requires a measurement device that is able to locally detect the state of the boundary layer in real-time. The intrinsic differences between the boundary layer states include the shear stress at the skin of the airfoil, the heat transfer between the air and the skin, and the increased high frequency pressure fluctuations [1]. Given these differences, various measurement techniques to be used in wind tunnel testing have been developed to determine the local state of the flow around the airfoil, such as pressure or sound transducers [9–11], hot film sensors [12–15], infrared radiation (IR) thermography [16–18], and shear stress measurements [19–22]. Pressure or sound transducers either measure the absolute pressure occurring at discrete locations on an airfoil, or rely on dynamic pressure fluctuations. Typical drawbacks of such measurements are the complication when multiple aerodynamic phenomena, such as transition and separation, coincide, as they provide similar pressure signatures. Hot film sensors and IR thermography rely on the fact that turbulent flow has a higher heat transfer capacity compared to laminar flow. Drawbacks of these measurements are the long minimal measurement time required and the need for active heating. Using shear stress measurements laminar, turbulent and separated flow can be measured as they all cause different magnitudes of shear stress to occur acting on the airfoil. The challenge here is the extremely low magnitude of the stresses to be measured as well as the reliance on delicate and damage-prone hot-film sensors [21, 22].

A promising and robust alternative sensor material which is capable of detecting dynamic pressure fluctuations are piezoelectric materials. These materials directly generate an electric signal as response to a dynamic mechanical stress [23]. While they experience the same drawbacks as other pressure based sensors, their high frequency bandwidth can be used to distinguish among various aerodynamic phenomena. Although their generated output voltage is generally rather low, specific mechanical boundary conditions can be applied to mechanically amplify the input force signal and hence, obtain significantly enhanced output voltages. An example of such passive amplification also utilised in the present work, is the use of a so-called bimorph, which in essence is a piezoelectric element clamped on one end, while the mechanical force is applied to the other end. Using this method, the output voltage and signal-to-noise ratio can be increased by an order of magnitude, while the (undesirable) pyroelectric contribution is suppressed [24].

While we here target a specific application, piezoelectric materials are not uncommon for use in wind-driven applications. Typical examples are flags or inverted flags for energy harvesting applications [25, 26], or the use of a piezoelectric bimorph as flow rate sensor [27]. Another example more applicable to the application envisioned in this paper demonstrates the use of piezoelectric bimorphs for measuring low shear stresses in typical fluid flow [20]. In that set-up two

piezoelectric bimorphs were mounted in parallel, with their tip connected to a rigid plate of a few square centimetres area. By applying a force parallel to the plate, pressure fluctuation values as low as one Pascal were measured, which is well within range of shear stresses typically found in boundary layers. Other research in this field involved the use of a piezoelectric composite bimorph of about 72 by 26 mm surface area, flush mounted on a flat plate acting both as a sensor and actuator [28]. While in sensor mode, the bimorph produced similar results to microphone sensors mounted on the same flat plate when tested in a wind tunnel.

While the first efforts in using piezoelectric bimorphs as flow sensors have shown promising results, such bimorphs would be used more optimally in case they were capable of detecting the large variety of boundary layer states. To date, no systematic effort has been spent on establishing these capabilities, neither for nominal (e.g. flat plate) nor more realistic aerodynamic geometries (e.g. airfoils). Considering an airfoil, the entire range of boundary layer states such as laminar, turbulent separating or attached can appear depending on the Reynolds number, angle of attack and shape of the airfoil. An effective sensor needs not only to locally detect flow fluctuations present in each of these states, but must be also coupled to an informed interpretation algorithm able to distinguish pertinent flow features.

In the present work we set the first step towards the generalisation of these piezoelectric bimorph sensors by conducting the first systematic study of their response to several boundary layer states developing on a typical airfoil. The aim of the work is not to develop a holistic sensing strategy (i.e. sensors, sensor placement, algorithms and implementations), rather to reconcile the output signal from an installed sensor to the incoming boundary layer. This forms the first step in characterising the envelop of this sensor and provides physical insights into the interpretation of the signals.

Two piezoelectric series bimorph sensors, including amplifiers, are installed within a NACA 0012 symmetrical airfoil commonly used in laminar and flow control studies [29, 30]. The piezoelectric sensors are located under the skin of the airfoil, and are attached to a vane piercing the skin to detect flow fluctuations or perturbations in the boundary layer. One sensor is located near the leading edge, while the other sensor is closer to the trailing edge. The local boundary state at each sensor was varied by systematically varying the angle of attack. Concurrent time-resolved particle image velocimetry (PIV) measurements performed on the same setup are used as validation technique. We show that a single data point obtained from the piezoelectric sensor is sufficient to define the state of the boundary layer.

2. Method

2.1. Piezoelectric sensors

Our in-house knowledge of piezoelectric materials enabled us to design our own piezoelectric bimorphs, providing excellent control over layer thicknesses, materials and poling conditions [31–36]. The procedure followed is typically used in

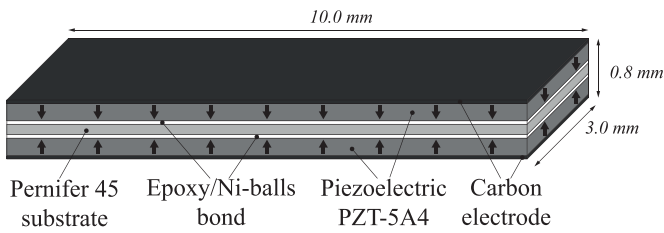


Figure 1. Layup and dimensions of the piezoelectric bimorph. The arrows in the PZT-5A4 plates indicate the poling direction which have to be pointed in opposite direction of each other.

industry to manufacture piezoelectric bimorphs. First, commercially produced piezoelectric PZT-5A4 plates with a size of $74 \times 45 \times 0.25$ mm and silver electrodes on both sides were poled at 150°C under a 2 kV mm^{-1} DC electric field for 5 min. After poling, two PZT-5A4 plates were bonded to either side of a Pernifer 45 substrate using epoxy (Epotek epoxy 302-3 M, Epoxy Technology Inc.) containing 5 wt% Ni-balls with a diameter of about $10 \mu\text{m}$. The Ni-balls make the bond conductive, electrically connecting one of each of the PZT-5A4 electrodes to the conductive Pernifer 45 substrate. Both PZT-5A4 plates were bonded in such a way that the poling directions were opposing each other, meaning that both poling directions were either pointing towards, or away from, the Pernifer 45 substrate. This is critically important for a series bimorph to work, because this cancels the pyroelectric effect and adds, instead of subtracts, the voltages generated by the piezoelectric effect [23]. After bonding, the two free electrodes on the PZT-5A4 were covered in carbon paste, acting as a protective electrically conductive coating. Finally, the sandwich structure was sawed using a diamond blade to the desired size of 3 by 10 mm. This size was chosen in order to achieve a high enough resonance frequency, which in this case was measured to be nearly 3 kHz (this is including the mechanical constraints introduced by the enclosure discussed in the next paragraph). This way, because turbulent flow inherently possesses kHz vibrations while laminar flow does not, turbulent flow will amplify the natural frequency of the bimorph. The layup described in this paragraph is visualized in figure 1. The capacitance and dielectric loss were measured at 1 kHz and 1 V with an Agilent 4263B LCR meter (Santa Clara, CA, USA), and were found to be 900 pF and 0.02, respectively.

Using a 3D printer (Ultimaker 3, Ultimaker B.V., Utrecht, The Netherlands), a polylactic acid (PLA) enclosure was 3D printed to house the piezoelectric bimorph. About 2 mm of the piezoelectric bimorph length was clamped in one of the walls of the enclosure, leaving a free length of 8 mm. On the free end of the piezoelectric bimorph, a 3D printed PLA vane was glued using cyanoacrylate adhesive. This vane was installed such to protrude through an opportune opening in the skin of the airfoil to mechanically couple the external flow to the piezoelectric bimorph. The vane reached a height of about 1.7 mm above the airfoil skin, and had a width of 6.0 mm. We purposely tailored the height of the vane to be this large in order to cover at least the entire (expected) boundary layer thickness. The width of the vane was also chosen to be relatively large in order

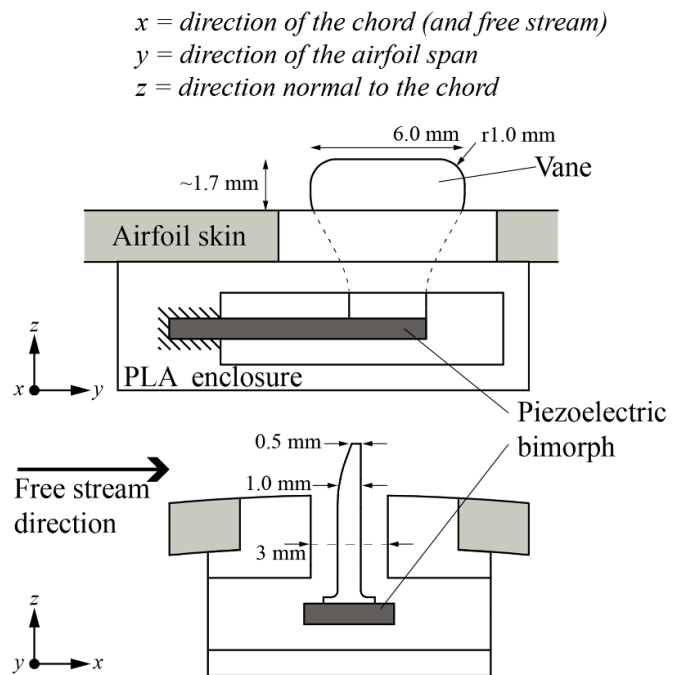


Figure 2. Schematic representation of the piezoelectric bimorph inside a PLA enclosure mounted underneath the airfoil skin. The vane is piercing the skin to transfer the oscillations originating from the boundary layer to the piezoelectric bimorph.

to increase the force acting on the bimorph, thereby increasing the signal-to-noise ratio. However, these dimensions used here are most likely on the large side, and future experiments are required to find optimal dimensions. Besides the width and height of the vane, the other dimensions were chosen taking into account the dimensions of the airfoil and the spaces left for mounting them. Rounded edges were introduced to limit strong disturbances in the surrounding flow. A schematic representation of the piezoelectric bimorph including the vane inside the enclosure is given in figure 2.

An ultra-low input current CMOS amplifier was directly connected to both carbon electrodes of the piezoelectric bimorph, providing a resistive load of $100 \text{ M}\Omega$. The amplifier copies the voltage obtained from the piezoelectric bimorph, amplifies it, and drives a data acquisition unit without signal loss due to wiring and circuit load. To minimise environmental noise, the wires between the piezoelectric bimorph and amplifier were kept as short as possible. The amplifiers send the analogue signal to a data acquisition unit, which converts it to a digital signal, at a sampling frequency of 40 kHz. The used data acquisition hardware has a built in anti-aliasing filter which requires one to measure about ten times higher than the highest desired frequency to measure. We were therefore able to measure accurately up to 4 kHz.

A NACA 0012 airfoil with a chord length of 200 mm and a span of 400 mm was used for the characterisation of two separate sensors. We chose to go for two sensors in order to have one measuring a transition without a laminar separation bubble (LSB), which on a NACA 0012 airfoil typically occurs near the LE, and one measuring a transition with LSB, which

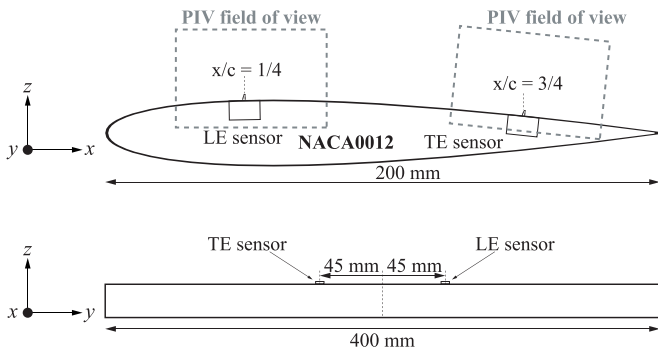


Figure 3. Schematic representation of the locations of the piezoelectric sensor located near the LE and the TE of the airfoil. The top image shows the side view with the chordwise locations, including a representation of the respective PIV fields of view, while the bottom image shows the view from the LE with the spanwise locations.

typically occurs near the TE. These positions are shown in figure 3. To prevent the turbulent wedge created by the LE sensor to influence the measurements taken by the TE sensor, the two sensors were positioned 45 mm on either side of the mid-span of the airfoil.

It must be noted that, although the manufacturing was performed as accurately as possible, the actual dimensions of the piezoelectric bimorph and PLA enclosure can vary from sensor to sensor. This in turn can have an influence on the resonance frequency and sensor sensitivity. However, the primary objective of the sensor is to infer the state of the local boundary layer in its vicinity. As will be shown in subsequent sections, this can be performed in a relativistic manner, meaning that the exact values of the resonance frequency and sensor sensitivity are not crucial. The amplitude will be extracted from a range of frequencies, and hence, as long as the resonance frequency stays within the respective range, the exact value is not important. In addition, we do not require an exact amplitude measurement, as we only compare relative values. As such, a detailed uncertainty evaluation of the sensor is not deemed necessary for boundary layer state estimation.

2.2. Experimental setup

The wind tunnel experiments were performed in the A-Tunnel, at the Low Speed Laboratory of the Delft University of Technology. The A-Tunnel is a low turbulence tunnel with a turbulence intensity of below 0.1% and interchangeable exit nozzles [37]. For the present study, an open-jet exit nozzle with a cross section of 600 by 400 mm was used, allowing a maximum free stream velocity of about 35 m s^{-1} . The NACA 0012 airfoil was positioned in the midplane, approximately 200 mm from the exit nozzle. To ensure spanwise invariant conditions, flat side plates of 600 mm width and 1000 mm length were used. During the experiments this free stream velocity was monitored using a pitot-static tube located upstream of the airfoil. For the experiments reported here, the tunnel was operated at 12.5 m s^{-1} , corresponding to a chord Reynolds number of $165 \cdot 10^3$. The Reynolds number was calculated using a

kinematic viscosity, ν , of $1.5111 \cdot 10^{-5} \text{ m}^2 \text{ s}^{-1}$, and a characteristic length, L , of 200 mm, equal to the chord length of the airfoil. The airfoil angle of attack was digitally controlled and set using an automatic rotation table with a positional resolution of 0.1° . Furthermore, the boundary layer on the pressure side of the airfoil was tripped to turbulence using a zigzag tape. This eliminates any possible influence of pressure side separation on the suction side developing flow.

Time-resolved two-component planar PIV measurements were performed for the characterization of the boundary layer in the vicinity of the sensor. A Photron SA1.1 with a 1024×1024 pixel CMOS sensor was equipped with a 105 mm macro objective, set at aperture number of 5.6. A Quantronix Darwin Duo Nd: YLF high speed laser (30 mJ per pulse) was used in conjunction with a set of spherical and cylindrical objectives to form a laser light sheet of approximately 1 mm thickness. The laser sheet was aligned to the x - z plane and was positioned such as to intersect the mid of the piezoelectric sensor vane. Pairs of images were captured at 6 kHz sampling rate, over a total measurement time of about 1 s. Inter-pair time separation was set to $60 \mu\text{s}$, resulting in average particle displacement of approximately 14 pixels in the freestream. The flow was seeded with theatrical smoke produced using an atomised water-glycol mixture, resulting in tracer particles of about $1 \mu\text{m}$ diameter. Synchronisation of camera and laser as well as image acquisition was performed using LaVision Davis software.

The flow developing in the vicinity of the LE and TE sensor was imaged independently. A field of view of approximately $90 \times 45 \text{ mm}$ was imaged, with a magnification factor of approximately 0.08. Particle image pairs were processed using multi-pass correlation algorithms in Lavision Davis 10 software. A final interrogation window of 16×16 pixels and 75% overlap was used, producing a final vector spacing of $88 \mu\text{m}$. The random error in the instantaneous velocity fields is estimated to be less than 1% [38].

Using the PIV data, two boundary layer thicknesses were calculated being the displacement thickness, δ^* , and the momentum thickness, θ [1, 2]. These thickness can be calculated using:

$$\delta^* = \int_0^{y_{\max}} \left(1 - \frac{u(y)}{u_\infty}\right) dy \quad (1)$$

$$\theta = \int_0^{y_{\max}} \frac{u(y)}{u_\infty} \left(1 - \frac{u(y)}{u_\infty}\right) dy. \quad (2)$$

In here, y_{\max} is the value of y where the local external (i.e. outside the boundary layer) velocity ($u_\infty = u(y = y_{\max})$) is reached, and $u(y)$ is the boundary layer velocity in the x -direction.

2.3. Test cases

Prior to the PIV measurements, the output of both piezoelectric sensors was measured over a time period of 10 s in static

Table 1. Imposed angles of attack for the concurrent PIV and piezoelectric sensor measurements.

	LE sensor	TE sensor
Angle of attack, α , ($^{\circ}$)	1	1
	4	2
	6	3
	6.5	4
	7	5
	7.5	6
	8	13
	8.5	16
	9	
	13	
	16	

conditions (i.e. at a constant freestream velocity and angle of attack). These measurements were taken at angles of attack from 0° to 18° , with a step size of 0.5° . The measured data was analysed in Fourier space using Welch's method, splitting the data into 20 segments with a 50% overlap [39]. The power spectral density (PSD) of the signal is calculated at discrete frequencies with a resolution of 20 000 data points. The PSD is further scaled by the equivalent noise bandwidth of each window in order to arrive at an estimate of spectral power at each frequency (given in dB).

The PIV measurements were performed on one of the two piezoelectric sensors at a time to achieve higher spatial resolution. Concurrent with each PIV measurement, the output of the piezoelectric sensor was also measured. The angles of attack for which PIV acquisitions were made were chosen based on the piezoelectric data obtained earlier, such to reveal pertinent features underlying the developing flow. Additional angles with a small step size were taken in regimes of strong variations of phenomena. The imposed angles of attack for both sensors are listed in table 1.

3. Results

3.1. Piezoelectric data

Figure 4 shows the spectral analysis of the piezoelectric sensor measurements which were measured prior to the PIV synchronized measurements. The PSD of the data is shown versus the frequency, f , for a large range of angles of attack, α . As earlier mentioned, the raw voltage data obtained from the piezoelectric sensors are analysed using Welch's method to obtain the frequency domain results, divided into results obtained using the LE sensor and the TE sensor. The row of peaks just below 3 kHz occurs due to the resonance frequency of sensor.

Figures 4(b) and (d) show the same data as in figures 4(a) and (c) but now in the form of contour plots to easily distinguish among the different regimes found. Figure 4(b) shows the measurement of the LE sensor, and shows three major regimes of angles of attack respectively named 'regime a' through 'regime c'. For the LE sensor, regime a extends to

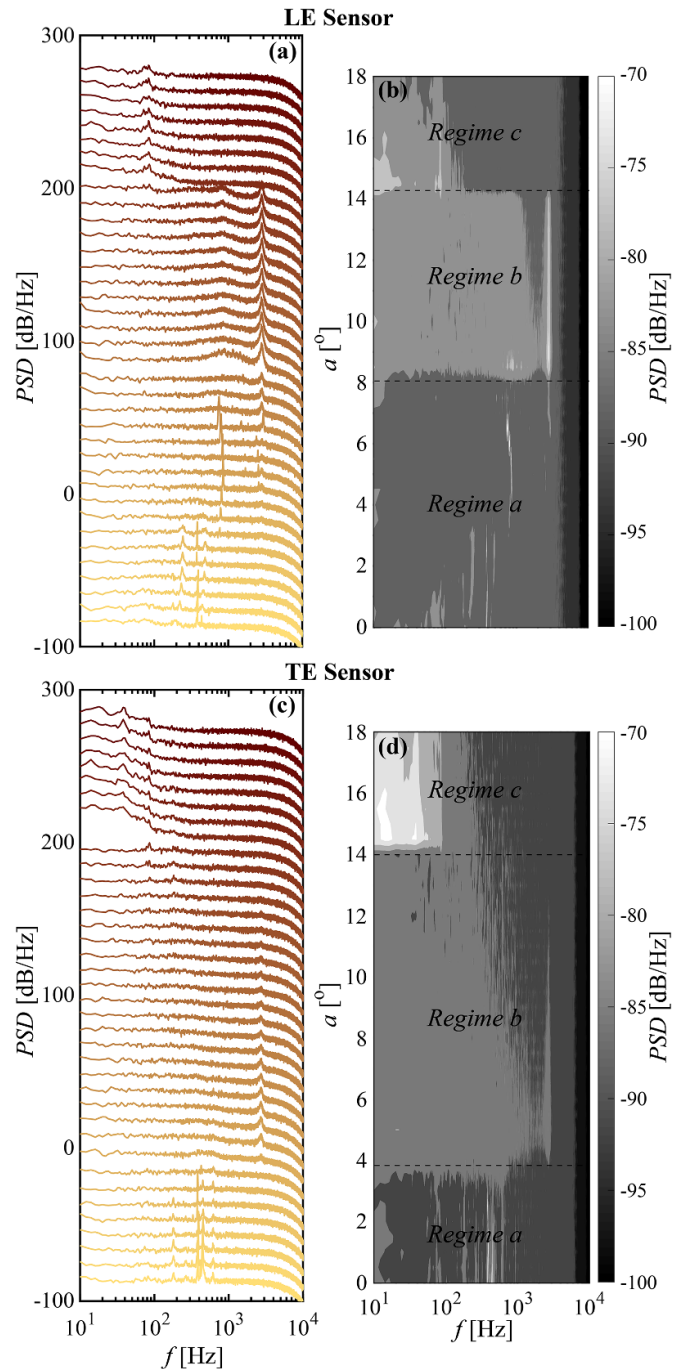


Figure 4. PSD versus frequency, f , as a function of angle of attack, α . LE sensor data plotted as (a) separated lines and (b) contour plot. TE sensor data plotted as (c) separated lines and (d) contour plot. For clarity, the lines in (a) and (c) are shifted by 10 dB Hz^{-1} per 0.5° angle of attack increase.

an α of about 8° , were relatively little activity is present. In regime b, which occurs between about 8° and 14° , the amplitude over the entire range of frequencies increases, with additional sharp peaks just below 3 kHz. Finally in regime c, above 14° , only a broad range of low frequency activity is observed below 100 Hz, while minimal activity is observed above this frequency. Figure 4(d), providing the measurements of the

TE sensor, reveals a similar regime distribution. The main difference is the border between regime a and b, which in this case lies around 4° .

In summary, figure 4 confirms the ability of the piezoelectric bimorph sensor to detect a wide range of events, occurring in distinctly different frequency bands. The dependence of these frequencies on the angle of attack suggests that indeed the sensor is activated by coherent fluctuations in the local flow. In the following sections we will use the time-resolved PIV measurements to identify these fluctuations as well as to infer the local boundary layer state.

3.2. Statistical velocity fields

Figure 5 shows an overview of the velocity fields obtained through the PIV measurements also showing the airfoil surface contour and the outline of the sensor. Velocity vectors are time averaged over the full measurement period. The contours of the data points having a negative velocity in the x direction, or negative u , are marked by the blue contour line to highlight reversed flow. The grey scale background presents the normalized standard deviation of velocity fluctuations of u (white background corresponds to standard deviation as for undisturbed flow, dark background corresponds to high standard deviations as for disturbed flow).

Figure 5(a), which shows the velocity field near the LE sensor, indicates a large wake behind the sensor vane up until 7° , which is considerably reduced at 13° angle of attack. This happens because transition at or near the site of the sensor vane occurs at an angle of attack around 8° . Hence, a developed turbulent flow exists above this angle, which suppresses separation, enhances mixing and results in a smaller wake. At 16° , massive flow separation (i.e. airfoil stall) occurs over the entire airfoil. Interestingly, the effect of the vane on the upstream flow field is rather small, indicating that the vane records the naturally occurring flow phenomena, rather than induces artificial flow phenomena related to the presence of the vane itself.

Taking a look at figure 5(b), which shows the velocity field near the TE sensor, a region of reversed flow upstream to the vane is observed at 1° . This is a typical manifestation of a LSB for this airfoil [30]. Furthermore, the LSB moves upstream at an angle of attack of 4° . We also note the reduced wake behind the sensor at an angle of 4° compared to the 1° case, again indicating a turbulent flow. At higher angles this wake increases again, up until separation happens at an angle of 16° .

4. Discussion

4.1. Boundary layer state from PIV

The state of the boundary layer can be extracted from the statistical PIV measurements in various ways. First, we consider the values of the standard deviation, σ , occurring in the flow. As shown in the previous section, the boundary layer develops a characteristic topology of velocity fluctuations near the

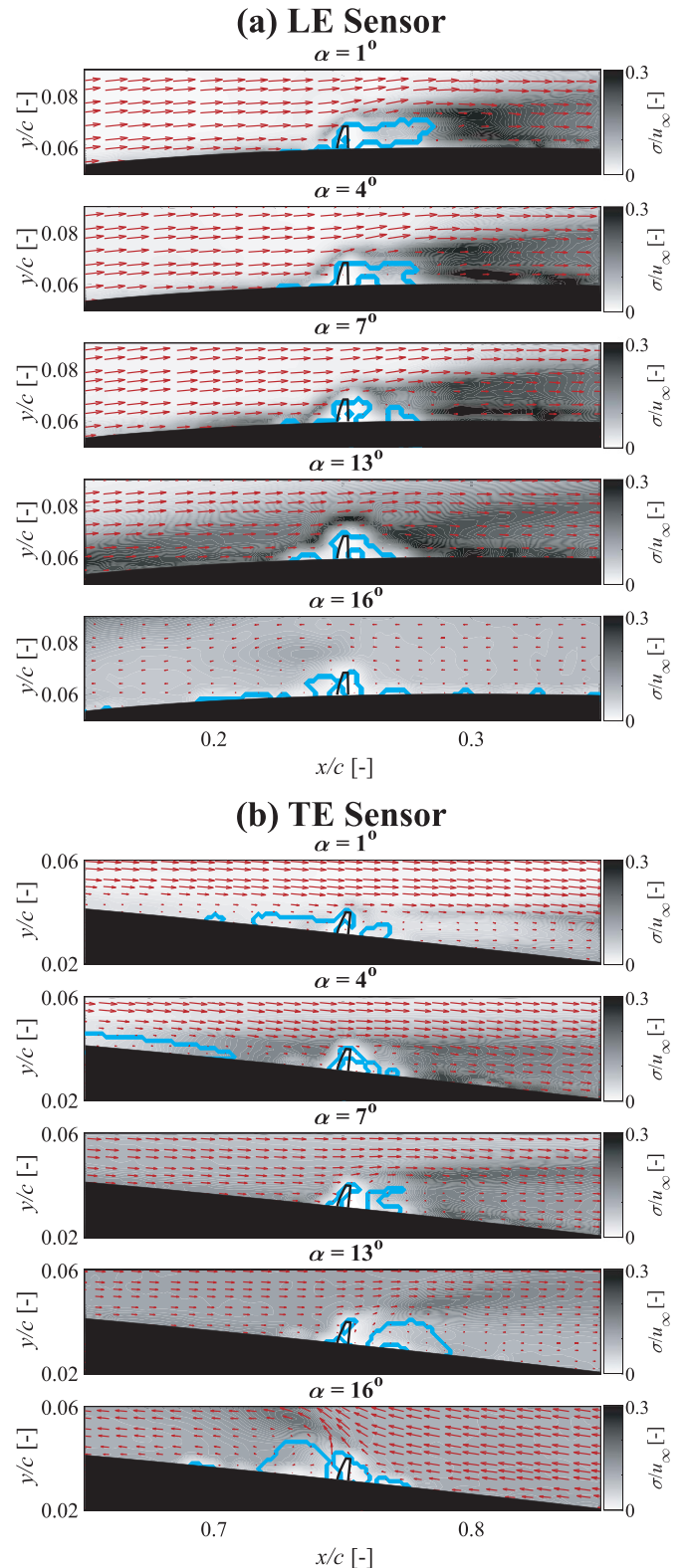


Figure 5. Processed PIV images with the piezoelectric sensor vane drawn in it, showing the time averaged velocity fields over the full measurement time, varying the angle of attack, α , of the sensor mounted near the (a) LE and (b) TE. The red arrows show the flowfield, the blue lines the contour of reversed flow, and the grayscale background the normalized standard deviation.

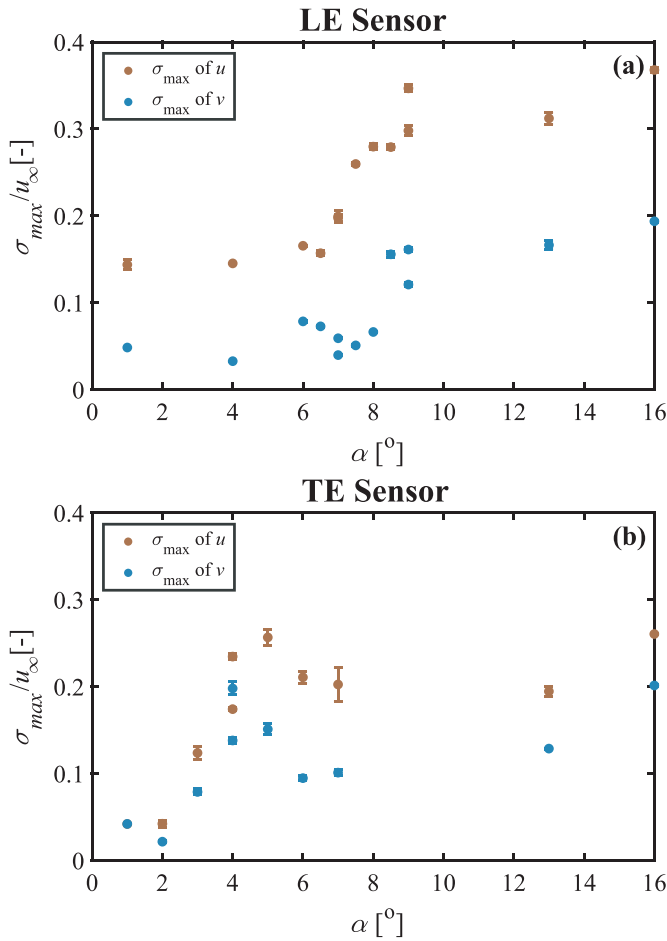


Figure 6. Maximum standard deviation values both the u and v vector versus the angle of attack, α , measured near the (a) LE sensor and (b) TE sensor. The values are extracted at an x -coordinate 4 mm upstream of the piezoelectric sensor.

wall and in the vicinity of the piezoelectric vane. Generally, the value σ in a turbulent flow is higher compared to a laminar flow, and peaks around transition, due to the appearance of large coherent structures prior to breakdown [10]. To facilitate proper comparison of cases at different angles of attack we choose an x -coordinate upstream of the sensor to probe the maximum σ in the boundary layer. We choose the probing location such that it lies sufficiently close to the sensor, yet is not directly affected by the sensor itself. By inspection of the fluctuation field topology for the majority of cases, the optimum probing location was found to be at $x/c = 0.23$ (LE sensor) and 0.73 (TE sensor), which corresponds to 4 mm upstream of the vane. At this x -coordinate, the maximum σ occurring through the entire y range was extracted per angle of attack for both u and v velocity components. The results are shown in figure 6.

In figure 6(a) the results near the LE sensor are shown. Both u and v fluctuations show a similar trend, having a relatively low value at low angles, peaking near 8.5° to 9°, and then continue to stay at a higher value compared to before the peak. Typically, the observed evolution of fluctuations confirms expectations on the development of transition, as the latter moves upstream with increasingly adverse pressure

gradient (i.e. increasing angle of attack). Based on these observations, transition from laminar to turbulent flow at the probe location is occurring at the site of the LE sensor in the range of angles of attack between 8.5° and 9°. Figure 6(b) shows the results near the TE sensor, and reveals a corresponding fluctuation peak at 4° to 5°.

A second independent evaluation of a boundary layer state can be made based on the consideration of integral quantities, such as momentum and displacement thickness, and their respective ratio (i.e. the so-called shape factor). A boundary layer in turbulent state will possess less momentum compared to a respective laminar state due to increased wall shear. This will directly entail a larger momentum thickness. Similarly, due to less momentum, a turbulent boundary layer will also thicken, displacing the outer inviscid streamlines more than when laminar. This will correspond to an increase in displacement thickness. However, due to the increased mixing in a turbulent boundary layer, momentum is largely redistributed in the layer, causing the two thicknesses to increase differently. This results into a different shape factor (δ^*/θ) for laminar and turbulent boundary layers, with the latter begin typically lower ($H = \sim 1.4$ for turbulent vs. $H = \sim 2.6$ for laminar states in flat plate conditions). Considering the shape factor of a given boundary layer provides a robust estimate of its state, purely based on time averaged statistical velocity information.

For the present cases, the integral boundary layer thickness and resulting shape factors are estimated based on the PIV velocity measurements at an x -coordinate of 4 mm upstream of the sensor vane. The results are shown in figure 7.

Figure 7(a) gives the thicknesses found near the LE sensor, and shows thickening of the boundary layer near 8° to 9°, which is in good agreement with the increase of velocity fluctuations associated to transition. For the case of the TE sensor, the displacement thickness given in figure 7(b) shows an early peak around 3°, corresponding to the emergence of a LSB, visible in figure 5. The appearance of a LSB is well documented for the current airfoil and Reynolds number [30], and increases the complexity of the fluctuation flow as will be shown later. The momentum thickness further shows an increase around transition near an angle of 4° to 5°. Around 13° a major increase in thickness is observed, corresponding to the eminent global separation of the flow, as was earlier seen in figure 5. In addition, it becomes evident that in all cases the vane height is considerably larger than the incoming boundary layer thickness, with the exception of the massively separated flow at an angle of attack of 16°.

The results presented up to this point clearly indicated the ability of the used configuration to assume a wide range boundary layer states. Relatively wide ranges of angle of attack are defined in laminar or turbulent states, with a clear transition point while specific angles reveal the appearance of LSBs or fully separated flows.

4.2. Detection of boundary layer fluctuations

From the aforementioned observations it becomes clear that the piezoelectric bimorph sensor is exposed to a wide range of fluctuations in the identified angle of attack regimes. Similarly,

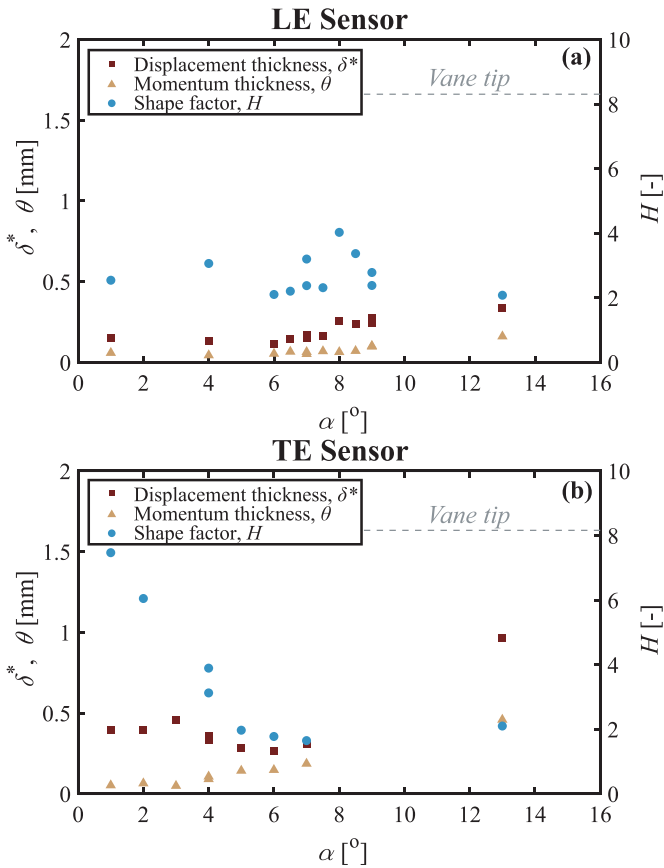


Figure 7. Boundary layer displacement thickness, δ^* , momentum thickness, θ , and shape factor, H , versus the angle of attack, α , measured near the (a) LE sensor and (b) TE sensor. The values are extracted at an x -coordinate 4 mm upstream of the piezoelectric sensor. The angles of incidence tested for the LE and TE were selected separately to get the most informative datasets for both.

the inspection of the PIV measurements allows proper identification of the boundary layer states as function of chordwise location and angle of attack.

Nevertheless, while the PIV measurements provide a spatio-temporal representation of the flowfield, the bimorph sensor essentially extracts a single time series of data, corresponding to the integrated mechanical force acting on the vane. In order to facilitate the comparison of the velocity fluctuations found in the PIV data to the unsteady output signal of the piezoelectric bimorph, a procedure is devised for the extraction of pertinent velocity information. The chosen method is not unique, however it was found to be effective in facilitating this comparison.

The extraction method is visualized in figure 8. First, we define xy -coordinates from which to extract u and v vectors. The x -coordinate is fixed at 4 mm upstream of the sensor vane, as this was found to be a sufficient distance to avoid measurement interference originating from the upstream effects of the sensor vane on the boundary layer. An exception was made for the case of an angle of attack of 16° , with the x -coordinate chosen on the downstream side of the vane due to the flow direction reversal, as can be seen in figure 5. The y -coordinate was chosen to be 1, 2 and 4 mm above the airfoil surface. Although

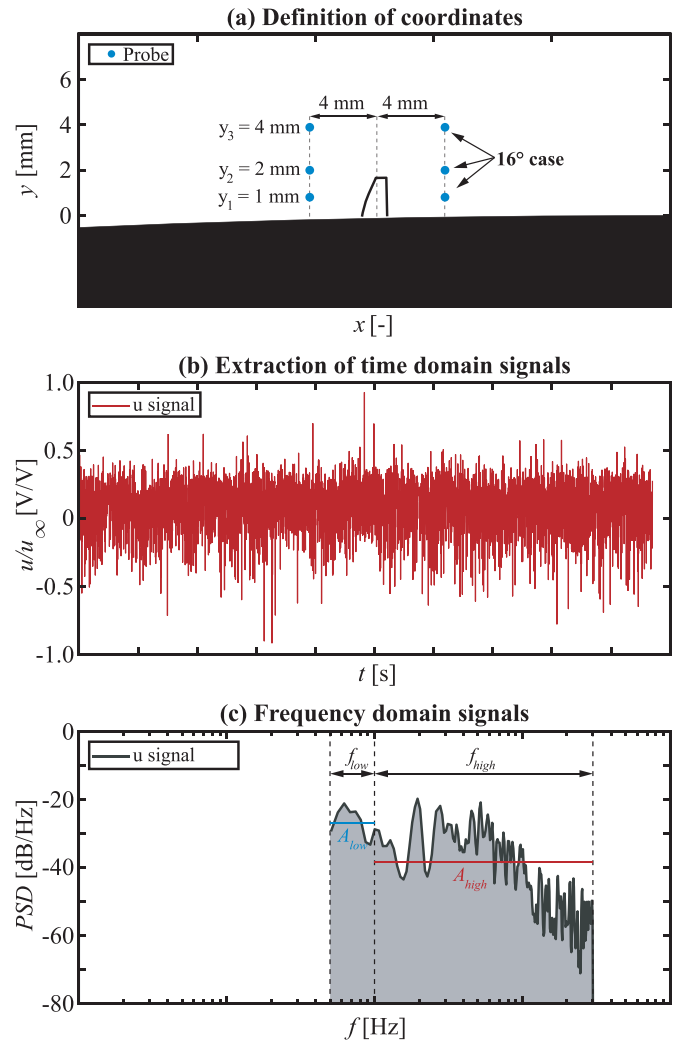


Figure 8. Method used to extract the oscillations occurring in the boundary layer from the PIV measurements. (a) Multiple probe coordinates are defined upstream of the sensor vane. (b) The time domain u signal is extracted from the probe coordinates. (c) Welch's method is used to obtain the frequency domain signal, and the power is calculated within two frequency bands.

for the majority of the cases the boundary layer is thinner than these values, lower y -coordinate locations were avoided due to areas of high light reflections, which reduce the confidence in the PIV data. The chosen xy -coordinates are visualized in figure 8(a).

The time series of the u vector component is extracted at each of the defined coordinates, as shown in figure 8(b). We use Welch's method to obtain the frequency domain signals. Two frequency bands of interest are defined based on the preceding analysis of the piezoelectric data (figure 4). The lower band is defined between 50 and 100 Hz. While considerable activity in the piezoelectric signal was present at frequencies as low as 10 Hz, the choice of a higher cut-off was made due to an artefact in the measurement routine. More specifically, the PIV laser was aligned to illuminate the mid-span of the vane, and as such it was found to intensively heat one side of the piezoelectric bimorph for a short time during acquisition. This caused a low frequency pyroelectric

contribution to the overall sensor output, which was largely suppressed by the choice of the frequency range boundaries. The higher band is chosen to be from 100 Hz to 3 kHz, which as mentioned earlier is the resonance frequency of the sensor assembly. By not including the resonance frequency, similar results are obtained. The main difference between including and excluding the resonance frequency, is the signal-to-noise ratio of the piezoelectric sensor signal. We therefore chose to include it.

The frequency bands are shown in figure 8(c). The total fluctuation amplitude within these frequency bands was calculated by integrating the frequency band within this range. The resulting amplitudes correspond to the statistical fluctuation strength within that particular frequency band occurring at the corresponding extraction location coordinate. Equivalent spectral analysis and frequency band definition was followed for the piezoelectric sensor data.

The outcomes of the spectral analysis method applied on both PIV and piezoelectric sensor data are visualized in figure 9 for the LE sensor. The low and high frequency bands are shown in figures 9(a) and (b) respectively. Each data point in the figure represents one PIV and one piezoelectric sensor measurement.

An evident dependence of the PIV fluctuation amplitude on the y -coordinate of velocity extraction can be observed for both low and high frequencies. While all three extraction probes reveal similar trends, one of the coordinate locations ($y = 2$ mm) reveals the closest agreement with the piezoelectric sensor output, as it shows a clear change in amplitude around transition located at an angle of about 8° – 9° . This is expected as the flow at $y = 2$ mm occurs in the vicinity of the tip of the vane, causing a larger momentum acting on the piezoelectric bimorph compared to the flow at $y = 1$ mm. The flow at $y = 4$ mm on the other hand is out of reach of the sensor vane. In general, both PIV and piezoelectric data signatures reveal low power values at angles below 8° , with an increase at higher angles. An outlier is present for the angle of 16° where only low frequencies remain, while high frequencies are largely dissipated. This was largely expected as at this angle of attack the location of the sensor vane is deeply in stagnant low velocity reverse flow, where high frequencies due to turbulent flow are absent [40].

Furthermore, a non-monotonic amplitude behaviour is observed in the high frequency band. More specifically, for the probe location of $y = 1$ mm, as well as for the piezoelectric sensor output, a local maximum is registered at angles of attack of 8° to 9° . This is attributed to two separate effects. Firstly, laminar-to-turbulent transition is occurring at these conditions in the vicinity of the sensor as shown in the previous section. For low Reynolds airfoils, transition is known to be forced by the appearance and amplification of coherent boundary layer instabilities such as Tollmien–Schlichting waves [8]. These reach maximum amplitude prior to turbulent breakdown. Furthermore, due to their spanwise coherency and narrow frequency band, the amplitude of these instabilities can well exceed turbulent fluctuations, thus producing local maximum evident in figure 9(b). Secondly, the boundary layer thickness increases at transition, as was seen before in figure 7,

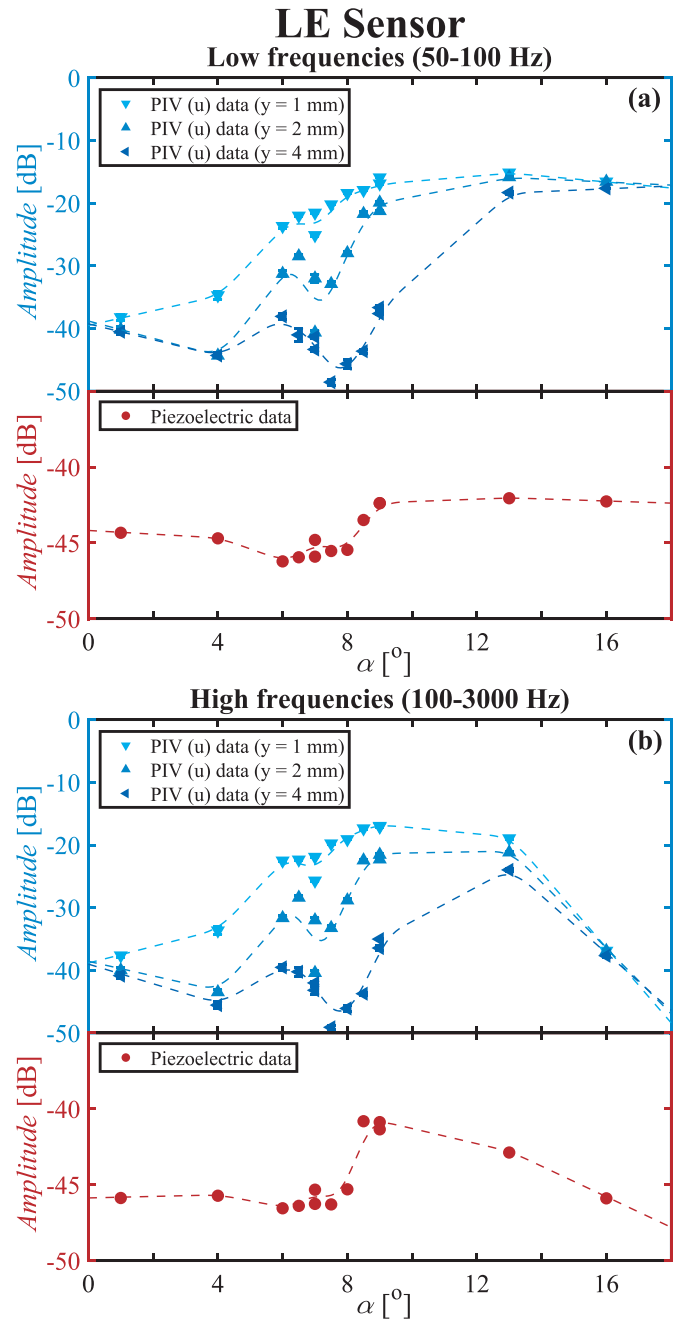


Figure 9. Power measured near the LE sensor of the piezoelectric and PIV data between (a) 50 and 100 Hz and (b) 100 and 3000 Hz. The PIV data is extracted from the coordinate about 4 mm upstream of the sensor vane and various y values above the airfoil skin. The general trends are shown by the dash lines, constructed by taking the moving average of the data.

effectively bringing the high fluctuation activity closer to the height of the piezoelectric vane as well as to the PIV probe locations.

In conclusion, the correspondence of piezoelectric sensor output to the PIV measurements is considerable, with strong similarities found in the evolution trend. The agreement further appears to be a function of the wall normal distance, as the sensor is evidently more sensitive to near-wall velocity fluctuations. The general sensing envelope of the LE sensor is

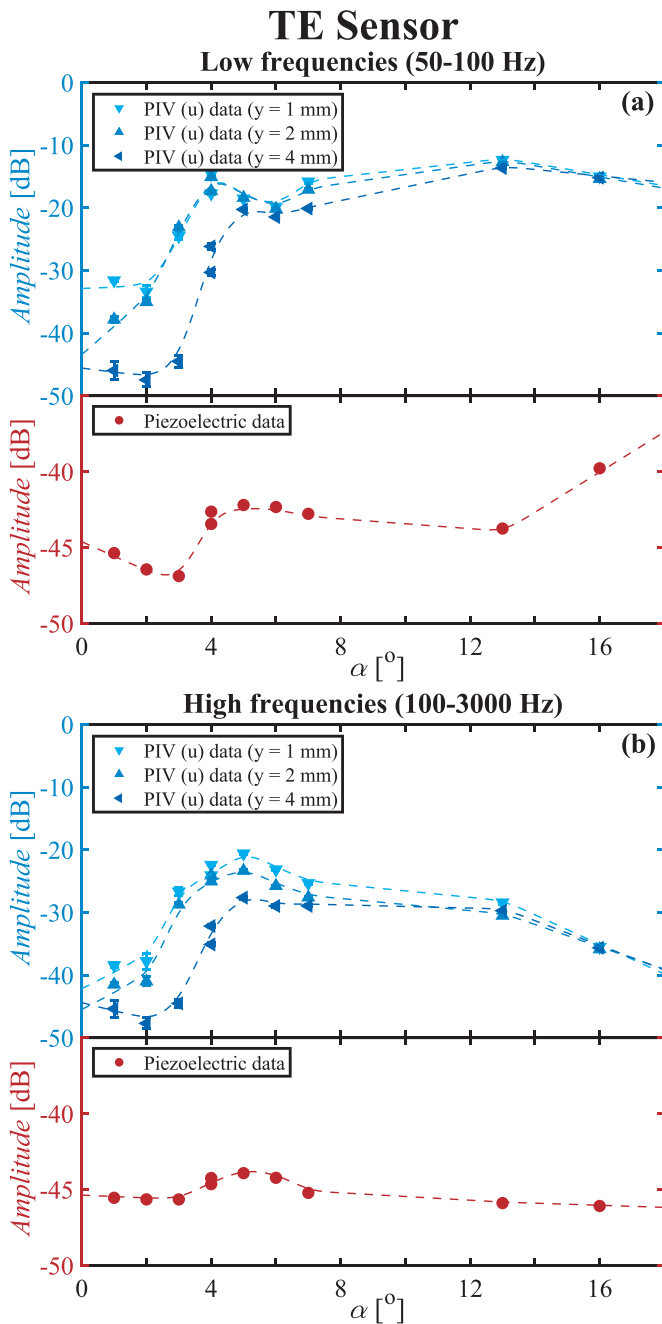


Figure 10. Power measured near the TE sensor of the piezoelectric and PIV data between (a) 50 and 100 Hz and (b) 100 and 3000 Hz. The PIV data is extracted from the coordinate about 4 mm upstream of the sensor vane and various y values above the airfoil skin. The general trends are shown by the dash lines, constructed by taking the moving average of the data.

characterised by low relative amplitudes in attached laminar flow (low angles of attack), high relative amplitudes in attached turbulent flow (high angles of attack), and considerable low frequency content at flow separation (angle of attack 16°). In addition, the sensor produces a characteristic maximum when the transition location corresponds to the vane position which happens at an angle of attack of 8.5° .

Figure 10 shows the corresponding comparison of the piezoelectric sensor output data and the data derived from the

PIV measurements for the TE sensor. The strong dependence of velocity fluctuations to wall normal probe location is similar to the LE sensor case. Again the output of the piezo sensor captures the same information as in the PIV signals. Yet, qualitative differences can be observed with respect to the readings of the LE sensor. Compared to the LE sensor, amplitude of the transition peak for the TE piezoelectric sensor is lower. This possible occurs due to the existence of the LSB near the TE sensor, as we saw earlier in figure 7, damping the effect of the transition peak. At an angle of 4° the downstream end of the LSB extends up until the sensor vane. The height of the vane enables it to still be able to pierce through the bubble thickness and ‘sense’ the external boundary layer flow. However, only the top portion of the vane is able to sense this, causing a lower overall mechanical input and hence a lower signal amplitude. Furthermore, another difference between the LE and TE case is the magnitude of the low frequency curves of both the piezoelectric output and PIV data. In the case of the TE sensor, stronger low frequencies occur near separation compared to the LE sensor. This simply occurs due to the stronger reversed flow observed near the TE sensor. This was already observed before at the 16° angle of attack cases in figure 5, where the flow velocity vectors at the TE sensor are clearly larger than those near the LE sensor.

In summary, the frequency intensities measured by the piezoelectric sensor correspond well to the fluctuations found in the boundary layer using PIV. In turn, these fluctuations can directly be related to the state of the boundary layer, indicating that the properly processed piezo sensor signal indeed can capture the state of the boundary layer.

4.3. How to read the piezoelectric sensor

The previous section has identified a clear relation between the boundary layer state and the piezoelectric sensor output. As mentioned in the introduction, the motivation for characterising this type of sensor in a wide range of flow conditions further serves in construction of a ‘response envelope’, which can be used for real-time and stand-alone interpretation of the sensor output as reference to the local boundary layer state. It has to be noted that the sensing ability of the sensor is strictly local and only refers to the boundary layer state at the location of the sensor. Based on the aforementioned analysis, this response envelope can be summarised as follows:

- *Laminar attached boundary layer:* the sensor output is mainly characterised by relatively low amplitudes at all frequencies.
- *Transition or eminent turbulent breakdown:* the sensor output indicates a maximum amplitude, specifically at high frequencies. Transition can be driven by classical boundary layer instabilities (i.e. TS waves) or through the formation of a LSB.
- *Attached turbulent flow:* the sensor registers considerable amplitude increase in both low and high frequencies. In addition the resonance frequency of the sensor (3 kHz for the present configuration) is strongly excited.

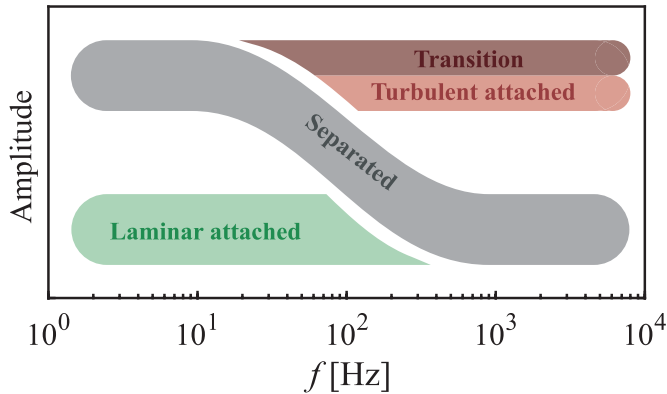


Figure 11. Response envelope of the piezoelectric sensor.

- *Massively separated flow*: the sensor registers increased fluctuation amplitude at low frequencies, but reduced amplitudes at high frequencies.

This response envelope is also summarised graphically in figure 11. It must be stressed that the general applicability of the envelope can be proposed for a relatively broad range of classical airfoil flows at low Reynolds numbers, as the NACA 0012 configuration in this work is fairly characteristic of these regimes. Nevertheless, for significantly different regimes such as encountered in swept wings, multi-element airfoils, high Reynolds or Mach numbers, careful calibration of the sensor response envelope against independent boundary layer state measurements should be performed. Furthermore, if the sensors are to be used outside the wind tunnel conditions, additional effects of changing temperature, humidity, pollution levels, added weight and sensor lifetime need to be taken into account as well. The current sensor design does not aim to reach a robust all-weather state but was developed to demonstrate the concept under the conditions as encountered in a wind tunnel. As such the dimensions and weight of the sensors and their wiring in a final real life application are expected to remain small, and not to lead to a serious weight penalty and or structural weakening of the airfoil.

Finally, the importance of the height of the sensor vane must be noted. If the vane is too small the mechanical input from the flow might be too low and the reach of the vane might not extend to important fluctuation events near the top of the boundary layer. On the other hand, if the vane is too large, it might not be sensitive enough to events near the root of the vane and the influence of the vane on the surrounding boundary layer might be excessive (i.e. increases fluctuations and/or forces transition). In the cases measured in this work the upstream and downstream effects of the sensor vane appeared to be minimal. In future, the optimal size of the sensor vane in relation to both measurement sensitivity and downstream effect should receive dedicated investigation for the corresponding conditions of full-scale applications.

5. Conclusions

This paper presents a piezoelectric bimorph sensor embedded in a NACA 0012 airfoil to measure fluctuations in the boundary layer. The objective was to prove that such a sensor can be used to distinguish among various boundary layer states.

Using PIV measurements as validation technique, we were able to show a clear relation between the piezoelectric sensor data and the boundary layer state. Dividing the signals into two frequency bands, the same signal signatures were found using the piezoelectric sensor and PIV measurements. Using the developed sensor response envelope, a single data point time series appears sufficient to specify the boundary layer state on classical airfoils in low Reynolds number regimes.

In the future, such a sensor might be used to map the boundary layer surrounding a more complex airfoil. It could also be used as an input component in a closed-loop control system to delay transition, and therewith reduce skin friction, possibly optimizing the overall lift-to-drag ratio of an airfoil.

Data availability statement

The data that support the findings of this study are available upon reasonable request from the authors.

Acknowledgments

The authors thank Ben Schelen for his expertise and design of the electronics for the piezoelectric sensor, and David Cannel of CeramTec for providing the piezoelectric PZT-5A4 plates. This work was part of the SmartX project at the Delft University of Technology. We thank Roeland de Breuker for his role in the project and involvement in this work. We like to state that the original concept of the piezo sensor was developed in collaboration with professor Pim Groen, who tragically passed away before the present validation experiments were conceived.

ORCID iDs

Vincent L Stuber  <https://orcid.org/0000-0002-6307-7369>

Marios Kotsonis  <https://orcid.org/0000-0003-0263-3648>

References

- [1] Schlichting H and Gersten K 2017 *Boundary-Layer Theory* (Berlin: Springer)
- [2] White F M 2006 *Viscous Fluid Flow* (New York: McGraw-Hill)
- [3] Gad-el-hak M 2001 Flow control: the future *J. Aircr.* **38** 402–18
- [4] Zhang Y, Fang X, Chen H, Fu S, Duan Z and Zhang Y 2015 Supercritical natural laminar flow airfoil optimization for regional aircraft wing design *Aerosp. Sci. Technol.* **43** 152–64

- [5] Cortelezzi L, Lee K H, Kim J and Speyer J L 1998 Skin-friction drag reduction via robust reduced-order linear feedback control *Int. J. Comput. Fluid Dyn.* **11** 79–92
- [6] Abbas A, Bugada G, Ferrer E, Fu S, Periaux J, Pons-Prats J, Valero E and Zheng Y 2017 Drag reduction via turbulent boundary layer flow control *Sci. China Technol. Sci.* **60** 1281–90
- [7] Grundmann S and Tropea C 2008 Active cancellation of artificially introduced Tollmien-Schlichting waves using plasma actuators *Exp. Fluids* **44** 795–806
- [8] Tol H J, De Visser C C and Kotsonis M 2019 Experimental model-based estimation and control of natural Tollmien-Schlichting waves *AIAA J.* **57** 2344–55
- [9] Gardner A D and Richter K 2015 Boundary layer transition determination for periodic and static flows using phase-averaged pressure data *Exp. Fluids* **56** 119
- [10] Özçakmak Ö S, Sørensen N N, Madsen H A and Sørensen J N 2019 Laminar-turbulent transition detection on airfoils by high-frequency microphone measurements *Wind Energy* **22** 1356–70
- [11] Popov A V, Botez R M and Labib M 2008 Transition point detection from the surface pressure distribution for controller design *J. Aircr.* **45** 23–28
- [12] Haghiri A A, Fallahpour N, Mani M and Tadjfar M 2015 Experimental study of boundary layer in compressible flow using hot film sensors through statistical and qualitative methods *J. Mech. Sci. Technol.* **29** 4671–9
- [13] Hausmann F and Schröder W 2006 Coated hot-film sensors for transition detection in cruise flight *J. Aircr.* **43** 456–65
- [14] Sturm H, Dumstorff G, Busche P, Westermann D and Lang W 2012 Boundary layer separation and reattachment detection on airfoils by thermal flow sensors *Sensors* **12** 14292–306
- [15] Sun B, Ma B, Wang P, Luo J, Deng J and Gao C 2020 High sensitive flexible hot-film sensor for measurement of unsteady boundary layer flow *Smart Mater. Struct.* **29** 35023
- [16] Mertens C, Wolf C C, Gardner A D, Schrijer F F J and van Oudheusden B W 2020 Advanced infrared thermography data analysis for unsteady boundary layer transition detection *Meas. Sci. Technol.* **31** 15301
- [17] Dollinger C, Sorg M, Balaesque N and Fischer A 2018 Measurement uncertainty of IR thermographic flow visualization measurements for transition detection on wind turbines in operation *Exp. Therm. Fluid Sci.* **97** 279–89
- [18] Gardner A D, Eder C, Wolf C C and Raffel M 2017 Analysis of differential infrared thermography for boundary layer transition detection *Exp. Fluids* **58** 122
- [19] Liu K, Yuan W, Deng J, Ma B and Jiang C 2007 Detecting boundary-layer separation point with a micro shear stress sensor array *Sens. Actuators A* **139** 31–35
- [20] Roche D, Richard C, Eyraud L and Audoly C 1996 Piezoelectric bimorph bending sensor for shear-stress measurement in fluid flow *Sens. Actuators A* **55** 157–62
- [21] Sun B, Wang P, Luo J, Deng J, Guo S and Ma B 2018 A flexible hot-film sensor array for underwater shear stress and transition measurement *Sensors* **18** 3469
- [22] Ghouila-Houri C, Talbi A, Viard R, Gallas Q, Garnier E, Merlen A and Pernod P 2019 High temperature gradient micro-sensors array for flow separation detection and control *Smart Mater. Struct.* **28** 125003
- [23] Holterman J and Groen P 2013 *An Introduction to Piezoelectric Materials and Applications* (the Netherlands: Stichting Applied Piezo, Apeldoorn)
- [24] Deutz D B 2017 *Flexible Piezoelectric Composites* (Delft, The Netherlands: Delft University of Technology)
- [25] Ovejas V J and Cuadras A 2011 Multimodal piezoelectric wind energy harvesters *Smart Mater. Struct.* **20** 85030
- [26] Orrego S, Shoele K, Ruas A, Doran K, Caggiano B, Mittal R and Kang S H 2017 Harvesting ambient wind energy with an inverted piezoelectric flag *Appl. Energy* **194** 212–22
- [27] Liu H, Zhang S, Kathiresan R, Kobayashi T and Lee C 2012 Development of piezoelectric microcantilever flow sensor with wind-driven energy harvesting capability *Appl. Phys. Lett.* **100** 5–8
- [28] Kumar V, Hays M, Fernandez E, Oates W and Alvi F S 2011 Flow sensitive actuators for micro-air vehicles *Smart Mater. Struct.* **20** 105033
- [29] Kotsonis M, Shukla R K and Pröbsting S 2015 Control of natural Tollmien-schlichting waves using dielectric barrier discharge plasma actuators *Int. J. Flow Control.* **7** 37–54
- [30] Yarusevych S and Kotsonis M 2017 Steady and transient response of a laminar separation bubble to controlled disturbances *J. Fluid Mech.* **813** 955–90
- [31] Deutz D B, Mascarenhas N T, Schelen J B J, de Leeuw D M, van der Zwaag S and Groen P 2017 Flexible piezoelectric touch sensor by alignment of lead-free alkaline niobate microcubes in PDMS *Adv. Funct. Mater.* **27** 1700728
- [32] Stuber V L, Deutz D B, Bennett J, Cannel D, De Leeuw D M, Van der zwaag S and Groen P 2019 Flexible lead-free piezoelectric composite materials for energy harvesting applications *Energy Technol.* **7** 177–85
- [33] Stuber V L, Mahon T R, van der Zwaag S and Groen P 2019 The effect of the intrinsic electrical matrix conductivity on the piezoelectric charge constant of piezoelectric composites *Mater. Res. Express* **7** 15703
- [34] Mkhoyan T, de Visser C and De Breuker R 2021 Adaptive state estimation and real-time tracking of aeroelastic wings with augmented kalman filter and kernelized correlation filter *AIAA Scitech 2021 Forum*
- [35] Khaliq J, Deutz D B, Frescas J A C, Vollenberg P, Hoeks T, van der Zwaag S and Groen P 2017 Effect of the piezoelectric ceramic filler dielectric constant on the piezoelectric properties of PZT-epoxy composites *Ceram. Int.* **43** 2774–9
- [36] Khanbareh H, van Der Zwaag S and Groen W A 2014 Effect of dielectrophoretic structuring on piezoelectric and pyroelectric properties of lead titanate-epoxy composites *Smart Mater. Struct.* **23** 105030
- [37] Merino-Martínez R, Rubio Carpio A, Lima Pereira L T, van Herk S, Avallone F, Ragni D and Kotsonis M 2020 Aeroacoustic design and characterization of the 3D-printed, open-jet, anechoic wind tunnel of Delft University of Technology *Appl. Acoust.* **170** 107504
- [38] Sciacchitano A, Neal D R, Smith B L, Warner S O, Vlachos P P, Wieneke B and Scarano F 2015 Collaborative framework for PIV uncertainty quantification: comparative assessment of methods *Meas. Sci. Technol.* **26** 74004
- [39] Welch P D 1967 The use of Fast fourier transform for the estimation of power spectra: a method based on time averaging over short, modified periodograms *IEEE Trans. Audio Electroacoust.* **15** 70–73
- [40] Broeren A P and Bragg M B 1999 Flowfield measurements over an airfoil during natural low-frequency oscillations near stall *AIAA J.* **37** 130–2